JOURNAL OF AIRCRAFT
Vol. 45, No. 3, May–June 2008

Drag Prediction for the DLR-F6 Wing–Body Configuration Using the Edge Solver

Peter Eliasson* and Shia-Hui Peng†
FOI, Swedish Defence Research Agency, 164 90 Stockholm, Sweden

DOI: 10.2514/1.31252

Numerical investigations are reported on the DLR-F6 wing–body configuration with and without fairing. The configurations have been adopted as test cases for the Third AIAA Drag Prediction Workshop. The addition of the fairing is to eliminate the flow separation bubble in the junction between the wing trailing edge and the fuselage. The computations have been carried out using two groups of unstructured grids with different sizes. In addition to the effect of incidences, studies of grid convergence have also been performed. The computational fluid dynamics solver Edge is used for the investigation. The calculations confirm that the flow separation can be removed in the wing-fuselage junction with the fairing. For this configuration, the results obtained with the two groups of grid are very similar. Without fairing, however, one group of grids has pronounced a lower lift and produced a more extended trailing-edge separation. Because no experimental data are available for the flow condition as specified in Drag Prediction Workshop-3, additional calculations have been carried out with the clean wing–body configuration at the Drag Prediction Workshop-2 Reynolds number to validate the numerical results against available experimental data. Very good agreement is obtained, in particular, for the global forces and moments. The calculation indicates that, as compared with experimental data, the grid which predicts a relatively large separation region provides improved predictions.

I. Introduction

THE investigation in this paper pursues further the work presented at the Second AIAA Drag Prediction Workshop (DPW-2) [1,2], where polar calculations and grid convergence studies were conducted for the DLR-F6 wing–body (WB) and wing–body–nacelle–pylon (WBNP) configurations. A summary of the results by the DPW-2 contributors was reported by Laflin et al. [3] with a statistical analysis by Hemsch and Morrison [4]. Since then, a number of numerical investigations on the DLR-F6 configuration have been reported, see, e.g., [5–12]. For DPW-3, only the DLR-F6 WB configuration is used, and the flow condition is changed with the Reynolds number increased from $Re = 3 \times 10^6$ (in DPW-2) to $Re = 5 \times 10^6$. Computations for an additional configuration are required in DPW-3, that is, the WB configuration with a fairing (WB-FX2B) added to the junction between the wing trailing edge and the fuselage with the intention to remove the flow separation in this region [13]. Because a new wind-tunnel test campaign has not yet taken place for the DPW-3 cases, numerical predictions have been presented with no comparison to experimental measurements. Nonetheless, with the same numerical procedure and the same turbulence model, we have performed a number of additional computations for the WB case (same geometric configuration for both DPW-2 and DPW-3) based on the DPW-2 flow condition (i.e., lower Re number compared to the DPW-3 specification), for which experimental data are available and have been used for comparison. This should allow a justifiable claim on the numerical procedure and turbulence modeling employed in present computations for the DPW-3 cases.

The emphasis in an earlier work related to DPW-2 was placed on the validation of different turbulence models [1,2]. In this paper, the turbulence model, which is able to produce improved predictions for the cases considered, has been selected. The model is a k-ω-based explicit algebraic Reynolds stress model (EARSM). To demonstrate the appropriateness of the selected turbulence model, some comparisons have also been made between the EARSM and the Spalart–Allmaras (SA) one-equation turbulence model. In our presentation at DPW-3, a set of subsequently refined unstructured grids provided by ANSYS with 3–20 million grid nodes were employed, where the results have been evaluated and compared with those computed by other contributors (http://aaac.larc.nasa.gov/tsab/cfdlarc/aiaa-dpw/). With the present work, one of the main purposes is to further investigate the effects of the faring, the grid refinement, and the Reynolds number. In addition, numerical results computed with a different set of unstructured grids generated by DLR with up to 10 million nodes are evaluated to study the effect of grid refinement and grid topology. The calculations with the DLR grids have been carried out after DPW-3 and the results are therefore not included in the submitted DPW-3 results [14], which are nevertheless presented in this work.

Although the focus of this work is on the analysis of numerical results obtained for DPW-3, some computations have also been performed with the DPW-2 conditions, by which the numerical settings and the grid sensitivity are explored in comparison with available experimental data.

In the following sections, the flow solver Edge is briefly introduced first, which is followed by a description of the numerical solution procedure and the turbulence models used in the computations. Proceeding with a presentation of the computational grids, numerical results for the WB configuration with the DPW-2 condition are validated in comparison with experimental data. The DPW-3 results are then presented and discussed, with a subsequent section of summary and conclusions of this work.

II. Numerical and Modeling Approaches

A. Flow Solver Edge

The computational fluid dynamics (CFD) solver employed in the calculations is the Edge code (http://www.foi.se/edge), which is an edge- and node-based Navier–Stokes flow solver applicable for both structured and unstructured grids [15,16]. Edge is based on a finite

Presented as Paper 897 at the 45th AIAA Aerospace Sciences Meeting and Exhibit, Reno, NV, 8–11 January 2007; received 27 March 2007; accepted for publication 17 June 2007.

*Deputy Research Director, Department of Computational Physics. AIAA Member.

†Research Director, Department of Computational Physics. AIAA Member.

volume formulation in which a median dual grid forms the control volumes with the unknowns allocated in the centers. The governing equations are integrated explicitly with a multistage Runge–Kutta scheme to steady state and with acceleration by full approximation storage (FAS) multigrid. A preprocessor creates the dual grid and the edge-based data structure, which is also employed to agglomerate coarser control volumes for the multigrid and to split up the computational domain for parallel calculations [17]. The Edge solver is able to provide different options, such as different spatial discretization techniques, turbulence models, and high-temperature extensions.

Four-level full multigrid W-cycles have been used in combination with a three-stage Runge–Kutta scheme. For the present calculations, a second-order central discretization of the convective terms is used for the mean flow with a small amount of artificial dissipation, which has been set to an optimal value so that the influence on the mean flow is negligibly small but large enough to maintain a stable numerical procedure for steady-state convergence. The normal derivatives of the viscous operator are discretized with a compact stencil [18]. The remaining derivatives are added based on node-based gradients to have a full viscous operator. The same settings have been applied in all calculations. All of the following results presented have reached good convergence with a reduction of more than five orders of magnitude in density residual by 1000–1500 multigrid iterations.

B. Turbulence Models

The computations have been carried out by assuming a fully developed turbulent flow. The effect of turbulence on the mean flow is modeled using an EARSM formulation based on a two-equation k-ω model [19]. For comparison, the Spalart-–Allmaras one-equation model [20] has also been employed in some computations. The turbulent transport equation is discretized with an upwind scheme, in which second-order accuracy is ensured by a total variation diminishing (TVD) limiter.

III. Results and Discussion

A. Computational Grids

Two groups of hybrid unstructured grids are employed in the computations, which have been generated by ANSYS and DLR, respectively. In the presentation at DPW-3, we presented only the results computed with the ANSYS grids. In this work, the DLR grids have also been invoked in the computations. Information about the ANSYS unstructured grid is provided in Table 1.

The ANSYS grids contain prismatic, pyramid, and tetrahedral elements. The maximum number of the near-wall prismatic layers is, in general, less than 31. A varying number is used and the number of layers is reduced in regions where the surface triangles are small due to resolution requirement, for example, at the trailing edge. The pyramids are used in the region of transition between prismatic and tetrahedral cells.

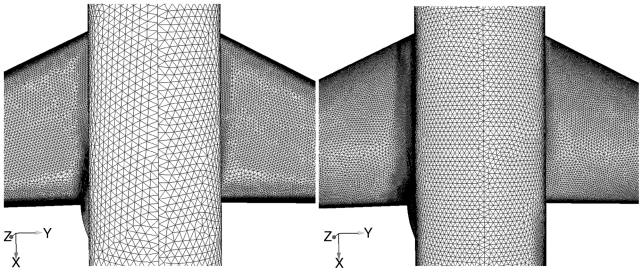

a) b)

Fig. 1 Surface grids for both WB (right-half plane) and WB-FX2B configurations (left-half plane). View at fuselage and inner wing: a) ANSYS medium grid, b) DLR fine grid.

The second set of unstructured grids has been provided by DLR, of which the information is given in Table 2. The DLR grids are somewhat similar to the ANSYS grids but are not so refined. The size of the fine DLR grids corresponds approximately to the size of the ANSYS medium grids. The DLR grids contain only prismatic and tetrahedral elements, because a constant number of near-wall prismatic layers are used and consequently pyramids are not required. The wall distance for the first node is not as small as with the ANSYS grids, but it is fine enough to ensure in general the first near-wall node being located in the viscous sublayer with $y^+ \leq 1.5$. Note also that the wall distance to the first node is about the same for all grids from the coarsest to the finest.

The surface grids and a cutting of the grid over a wing section are shown, respectively, in Figs. 1–3, in which the ANSYS medium grids are compared with the DLR fine grids. In Fig. 1, the fairing is clearly illustrated being attached over the junction of the fuselage and the wing trailing edge. Note that, in Fig. 1, for both ANSYS and DLR grids, the WB and WB-FX2B configurations have been placed in the same illustration on the left-hand (WB-FX2B) and right-hand (WB) side, respectively. Figure 2 presents a close-up view on the surface grid over the wing–body junction near the wing trailing edge. With similar numbers of grid nodes in total, and over the surface for the ANSYS medium and DLR fine grids, the two sets of wing surface grids have similar resolution but the clustering differs to some extent. Both grids have placed a clustered grid in the wing–body junction and along the leading edge. The DLR fine grid has a slightly more refined mesh over the wing–body junction than the ANSYS medium grid. The ANSYS grid, on the other hand, has a more extended grid refinement around the junction between the fuselage and the wing trailing edge, as seen in Fig. 2. Apart from regions around the wing–body junction and the leading and trailing edges of the wing, the

Table 1 Information about the unstructured grids from ANSYS

	Wing–body configuration, WB			Wing–body–fairing configuration, WB-FX2B		
Grid	coarse	medium	fine	coarse	medium	fine
No. of nodes	3.05×10^6	8.04×10^6	18.1×10^6	3.16×10^6	8.27×10^6	20.5×10^6
No. of bound. nodes	75×10^3	168×10^3	329×10^3	79×10^3	179×10^3	375×10^3
No. of prism layers	≤ 31	≤ 31	≤ 31	≤ 31	≤ 31	≤ 31
First normal cell size	0.6×10^{-6} m	0.4×10^{-6} m	0.25×10^{-6} m	0.6×10^{-6} m	0.4×10^{-6} m	0.25×10^{-6} m

Table 2 Information about the unstructured grids from DLR

	Wing–body configuration, WB			Wing–body–fairing configuration, WB-FX2B		
Grid	coarse	medium	fine	coarse	medium	fine
No. of nodes	2.46×10^6	5.10×10^6	8.54×10^6	2.87×10^6	6.11×10^6	10.3×10^6
No. of bound. nodes	45×10^3	86×10^3	122×10^3	60×10^3	113×10^3	167×10^3
No. of prism layers	21	31	40	21	31	40
First normal cell size	$\sim 1.0 \times 10^{-6}$ m	$\sim 1.0 \times 10^{-6}$ m	$\sim 1.0 \times 10^{-6}$ m	$\sim 1.0 \times 10^{-6}$ m	$\sim 1.0 \times 10^{-6}$ m	$\sim 1.0 \times 10^{-6}$ m

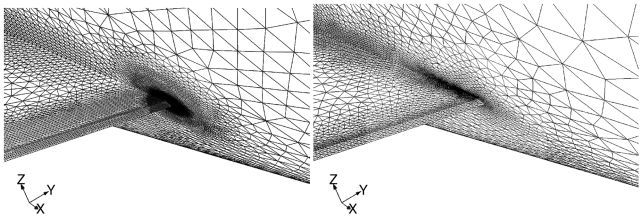

a) b)

Fig. 2 Surface grid for WB configuration. Close-up view of the grid at the wing trailing edge and fuselage junction: a) ANSYS medium grid, b) DLR fine grid.

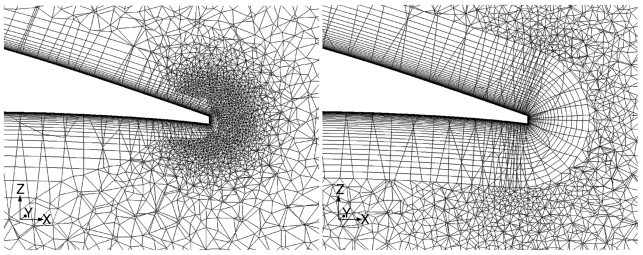

a) b)

Fig. 3 Grid cut at 15% wing span, WB configuration: a) ANSYS medium grid, b) DLR fine grid.

surface triangles are distributed fairly isotropically, with a slightly finer resolution for the DLR fine mesh.

Figure 3 illustrates the grid cut at 15% wing span. It is shown that the ANSYS grid has a varying number of prismatic cells near the surface, which is reduced near the trailing edge, where the tetrahedral elements have been refined in the neighboring off-wall region. The surface grids are refined at the leading edge as well as along the trailing edge. The DLR fine grid resolves the trailing edge with about five nodes where the nodes are placed in a structured way with a moderate stretching of the triangles. About the same number of nodes is used at the trailing edge in the ANSYS medium grid but with isotropic triangles.

B. Wing–Body Configuration with DPW-2 Conditions

At DPW-2, the WB configuration was computed using two sets of unstructured grids for flow conditions of $M_\infty = 0.75$ and $Re = 3 \times 10^6$, for which the results were obtained with a group of old DLR grids [1,2]. The WB configuration has been revisited in this work with the new grids supplied for DPW-3. The purpose is to make some comparison and validation against available experimental data from the previous workshop to ensure that the numerical scheme and physical modeling are properly implemented in the code. There was

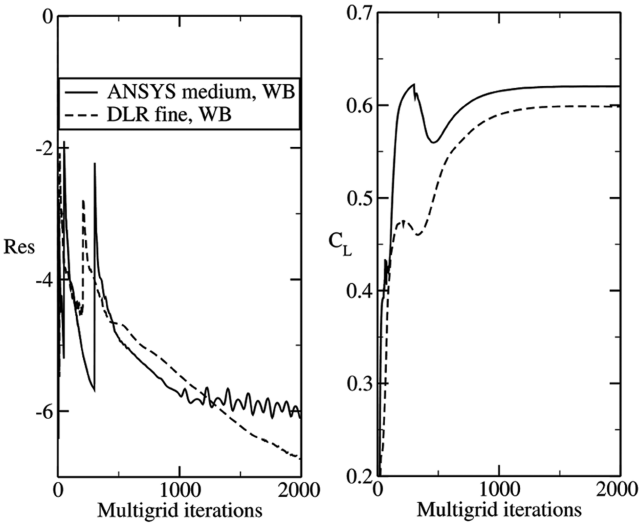

a) b)

Fig. 4 Illustration of solution convergence (WB configuration); $\alpha = 1.23$ deg and $Re = 3 \times 10^6$ with ANSYS medium and DLR fine grids: a) density residual, b) convergence of lift force.

also a wing–body–nacelle–pylon configuration at DPW-2, which is not considered in this work because it is no longer a specified test case for DPW-3.

The rate of convergence for the two grids is shown in Fig. 4. Both grids have rendered a good convergence rate for which the density residual is reduced by 6–7 orders of magnitude after 2000 multigrid iterations. The lift force has settled at a constant value after about 1500 iterations.

A sequence of eight angles of attack in the range of $\alpha \in [-3, 1.5$ deg] have been computed with the ANSYS and DLR medium grids. In addition, two angles of attack, $\alpha = -2$ and 1.23 deg, have also been computed on the coarse and fine grids of ANSYS and DLR, respectively, to investigate the grid dependency at low and high angles.

The integrated forces and moments are presented in Fig. 5 in comparison with experimental data. It is shown that the agreement between numerical and experimental values is satisfactory for both grids. The result obtained with the DLR grids produces, in general, an even better resemblance with the experimental values, as compared with the results obtained with the ANSYS grid. The lift is slightly overpredicted, in particular at the low angles of attack, which, however, matches well with the experimental data for $\alpha \geq 1$ deg with the DLR medium grid. The idealized drag profile illustrates that the numerical results with the DLR grid agree very well with the measured data, whereas the results with the ANSYS grid has somewhat overpredicted the drag at low angles. The pitching

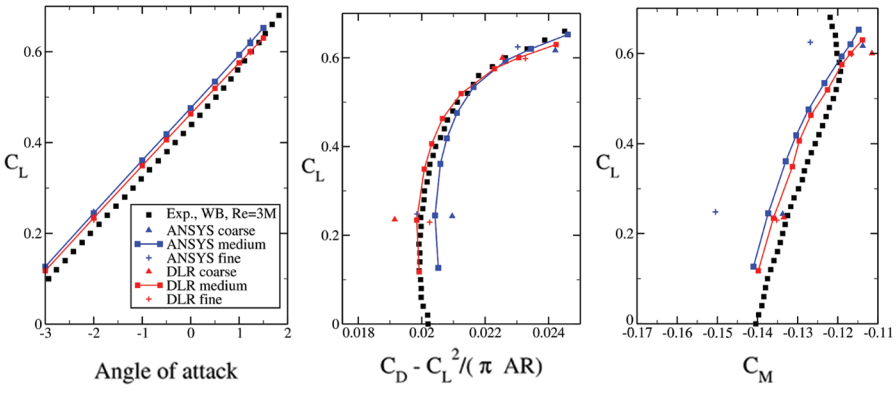

a) b) c)

Fig. 5 Integrated forces and moments for the WB configuration with ANSYS and DLR grids: a) C_L vs α, b) lift-drag polar with induced drag subtracted, c) C_L vs C_M. AR is the wing aspect ratio and AR = 9.5.

moment coefficient is one of the most difficult quantities for accurate numerical predictions. As shown in Fig. 5, nonetheless, the present computations have produced very encouraging numerical results for C_M, which is in rather good agreement with the experimental data, better than many other results reported previously for the same configuration. As with other numerical results, however, the prediction fails to reproduce the kink in the experimental curve at higher angles of attack.

The predicted lift is slightly larger with the ANSYS grids than with the DLR grids, on which the grid refinement has a negligibly small influence. The drag polar and the moment have shown to be more sensitive to the grid refinement, however. With the group of ANSYS grids, the grid refinement brings down the predicted drag at both angles computed, whereas the DLR grids have disclosed an opposite tendency. Both groups of grids present asymptotic grid sensitivity in the drag prediction, with an opposite direction though. For the pitching moment, a similar asymptotic grid sensitivity remains with the ANSYS grids, whereas the DLR grids have presented, to some extent, a sensible grid convergence from the medium to the fine grids. Although the difference between the solutions for two medium grids is small, the results on the ANSYS fine grid move away from the experimental values for the pitching moment and deviate more from the prediction with the DLR fine grid. In summary, two sets of solutions have been validated on two groups of unstructured grids. The solution obtained with the DLR grids provides better global forces and pitching moment than with the ANSYS grids. Grid refinement does not change the fact that the predicted lift is higher with the ANSYS grids.

Figure 6 displays the pressure distributions at four spanwise wing sections using the medium and fine meshes from both the ANSYS and DLR grids at $\alpha = 1.23$ deg. In general, with either the ANSYS or the DLR grids, the medium and fine meshes have produced very similar pressure distributions. The most obvious difference between the computed and experimental results is observed at the inboard station at 15% span, where a flow separation bubble arises in the wing–body junction near the wing trailing edge. Both sets of grids have produced C_p in some discrepancies from experimental data at this station. With a somewhat flat C_p distribution near the wing trailing edge, the results obtained on the DLR grids indicate a more extended separation area than predicted on the ANSYS grids, yet, at this section, the ANSYS grid renders a better agreement between the prediction and the experimental data over the range of about 80–100% of the local chord. At 60–80% chord, however, a lower pressure is predicted on the suction side, whereas the DLR grids have produced a pressure that is too high, but pronounced a low pressure in the vicinity of the trailing edge. At the outboard stations, the flow is attached and the difference between the computed results and experiments is reduced. The major difference is found in the predictions for the location of the shock, which has been reproduced reasonably well on the ANSYS grid, as compared with the experimental data. The prediction on the DLR grid has brought the shock location slightly upstream. This is observed at 24 and 41% of the wing span. At 64% wing span and beyond, the two sets of grids give consistent predictions for the shock location. In relation to the global forces, it can be justified that the difference observed in the predictions of integrated forces with the two groups of grids may be attributed to the predictions of the shock location, as well as of the flow separation over the wing–body junction near the trailing edge.

It is interesting to note that the DLR grid has produced pressure distributions with somewhat larger discrepancies from the experimental data than the ANSYS grid, but this set of grids is able to render better predictions for the integrated forces and moments. With the DLR grids, the prediction of an earlier shock location over nearly a half of the wing span may have helped partly to render a reduced lift. Moreover, at the inboard section (see, e.g., Fig. 6 at 15% wing span) immediately after the shock, the overpredicted pressure on the suction side may have also contributed to the difference in the lift predictions.

The predicted inboard separation is shown in Fig. 7 by plotting the surface friction pattern. The separation bubble is pronounced, being much more extended on the DLR grids than on the ANSYS grids. Furthermore, the separation region obtained with the DLR grids has shown a better grid convergence in terms of its size and shape. The solutions obtained with all the ANSYS grids have disclosed a very small and weak flow separation on the wing surface, which is not comparable to the experimental visualization and to our previous computations with different turbulence models on another set of grids [1,2]. With the ANSYS grid, the flow starts the separation on the body and the separation bubble interfaces only weakly with the boundary layer over the wing surface. The solutions obtained with the DLR grids, on the other hand, show a relatively extensive separation, which emanates from the wing–body junction. The size of the bubble, however, is somewhat larger than what has been visualized experimentally. A qualitative illustration on the bubble size will be given in the following section in comparison with the experimental observation.

A summary of the computed forces at $\alpha = 1.23$ deg is given in Table 3 in comparison with experimental data measured at $\alpha = 1.25$ deg. The results on the DLR grids agree very well with the measurements, particularly for the lift. The drag deviates with about five drag counts (on the fine grid) and the pitching moment (on the fine grid) differs only 3%. On the ANSYS grids, the lift is generally overpredicted by about 4%, and the drag is overestimated with about 13 drag counts on the fine grid. Nevertheless, the deviation due to the

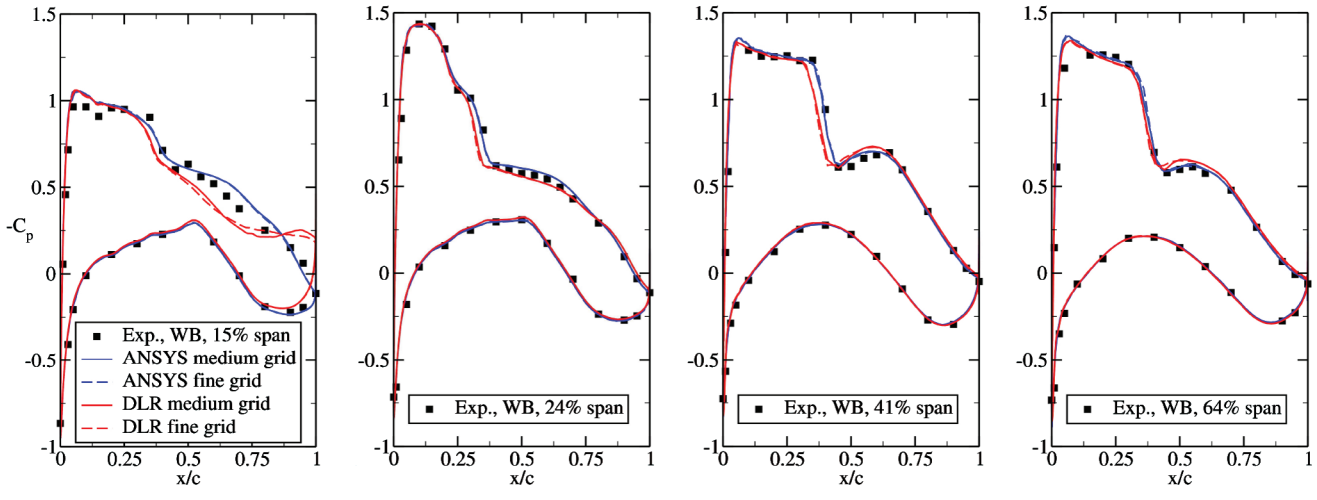

Fig. 6 Pressure distributions for the WB configuration on the ANSYS and DLR medium and fine grids, $\alpha = 1.23$ deg: a) 15% span, b) 24% span, c) 41% span, d) 64% span.

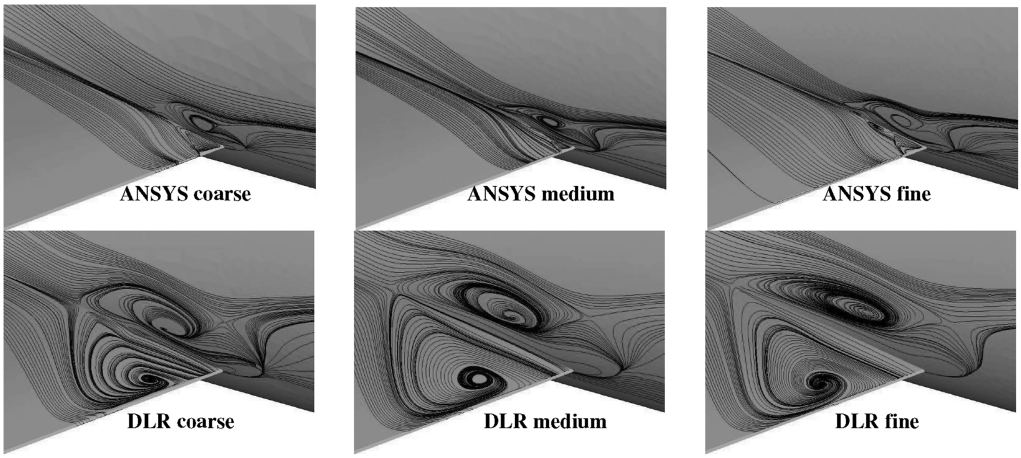

Fig. 7 Surface friction pattern at wing–body junction with the ANSYS and DLR grids, $\alpha = 1.23$ deg. Top: predictions with ANSYS grids. Bottom: predictions with DLR grids. From left to right: coarse, medium, and fine grids.

ANSYS grids is not so large as compared with other numerical results [3,4]. The differences between the predicted numerical results will be further analyzed and discussed in the next section for the DPW-3 computations.

In summary, the preceding computations based on the DPW-2 condition for the WB configuration have shown generally reasonable agreement with the experimental data. Using the same numerical settings and the same turbulence model, the present work suggests that the prediction of integrated forces and moments is less sensitive to the grid refinement within the same framework of a baseline grid, but may become rather sensitive to the grids generated on different platforms in terms of grid resolution on the surface and in some significant flow regions.

C. Numerical Results for DPW-3

Besides the wing–body configuration, a new configuration has been adopted as a test case for DPW-3, that is, the WB-FX2B configuration with a fairing added at the wing–body junction near the wing trailing edge, as shown in Fig. 1. The fairing is introduced to remove the separation in the junction [13]. The flow conditions have been changed by increasing the Reynolds number from $Re = 3 \times 10^6$ in DPW-2 to $Re = 5 \times 10^6$ in DPW-3. The Mach number remains the same with $M_\infty = 0.75$. Note that no experimental data are available for the DPW-3 flow conditions. Nonetheless, similar results are expected for the WB configuration in spite of different Reynolds numbers. The experimental data measured at $Re = 3 \times 10^6$ for this configuration may thus be taken as a reference for computations at $Re = 5 \times 10^6$. With the WB-FX2B configuration in DPW-3, it has been expected that the scattering in the WB results from the previous workshop should be alleviated by introducing a test case without separation.

Table 3 Integrated forces and moments at $\alpha = 1.23$ deg

Case	α, deg	C_L	C_D	C_M
ANSYS/WB coarse	1.23	0.6165	0.03695	−0.1138
ANSYS/WB medium	1.23	0.6203	0.03634	−0.1168
ANSYS/WB fine	1.23	0.6247	0.03610	−0.1268
DLR/WB coarse	1.23	0.5999	0.03460	−0.1115
DLR/WB medium	1.23	0.6004	0.03514	−0.1168
DLR/WB fine	1.23	0.5981	0.03526	−0.1166
Experiment	**1.25**	**0.6000**	**0.03470**	**−0.1202**

In all the computations for DPW-3, we have used the same numerical and physical settings as in the calculations for the WB configuration with the DPW2 conditions (in Sec. III.B). The convergence history is similar for both configurations at different Reynolds numbers. A grid refinement study is also required in DPW-3 and the subsequently refined grids, as shown, respectively, in Table 1 for the ANSYS grids and in Table 2 for the DLR grids, have been employed in the computations. Table 3 summarizes the predicted forces and moments on the four sets of grids. The angle of attack has been calibrated first with the medium grid such that the lift is $C_L \approx 0.5$. The same angle has then been used in the calculations for the coarse and fine ANSYS grids, although it has to be slightly modified to match $C_L \approx 0.5$ for the DLR fine grid (WB) and DLR coarse grid (WB-FX2B) (see Table 4).

The angle of attack for $C_L \approx 0.5$ is found in a narrow range of $\alpha = 0.04$–0.22 deg for the computed configurations and grids. For the WB configuration, a larger angle of attack is required to achieve $C_L \approx 0.5$ with the DLR grid than with the ANSYS grid. For the WB-FX2B configuration, by contrast, a slightly smaller angle is required with the DLR grid.

The convergence of the drag is plotted in Fig. 8 as a function of the number of grid nodes ($\sim N^{-2/3}$). The total drag has been further decomposed into two parts, the drag due to pressure and the friction drag. As observed in the computations for the WB configuration with

Table 4 Grid refinement study in predictions of integrated forces and moments, $C_L = 0.5$ approximately

Configuration	Grid	α, deg	C_L	C_D	$C_{D\,\text{pressure}}$	$C_{D\,\text{friction}}$	C_M
WB	ANSYS, coarse	0.04	0.4970	0.02856	0.01616	0.01240	−0.1324
	ANSYS, medium	0.04	0.5006	0.02800	0.01551	0.01249	−0.1366
	ANSYS, fine	0.04	0.5039	0.02763	0.01478	0.01285	−0.1474
	DLR, coarse	0.178	0.5003	0.02715	0.01634	0.01081	−0.1289
	DLR, medium	0.178	0.5005	0.02775	0.01592	0.01183	−0.1331
	DLR, fine	0.220	0.4993	0.02811	0.01584	0.01228	−0.1319
WB-FX2B	ANSYS, coarse	0.157	0.4968	0.02843	0.01608	0.01235	−0.1268
	ANSYS, medium	0.157	0.5002	0.02783	0.01540	0.01243	−0.1301
	ANSYS, fine	0.157	0.5020	0.02757	0.01508	0.01249	−0.1315
	DLR, coarse	0.195	0.4991	0.02697	0.01599	0.01098	−0.1280
	DLR, medium	0.093	0.5002	0.02731	0.01530	0.01201	−0.1349
	DLR, fine	0.093	0.4997	0.02746	0.01504	0.01242	−0.1339

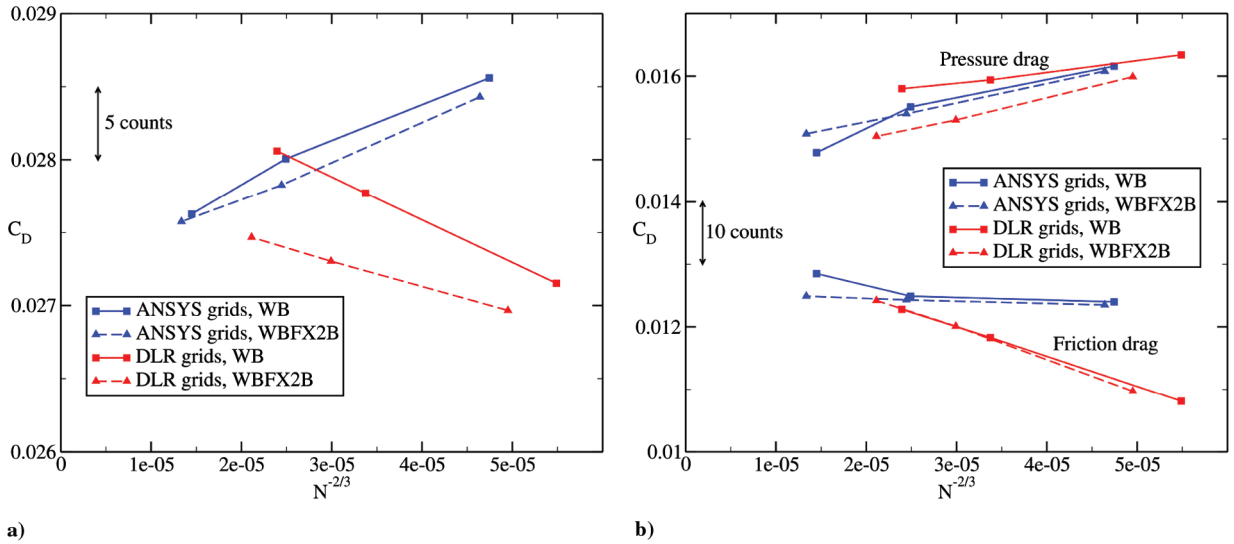

Fig. 8 Convergence of drag vs $N^{-2/3}$, where N is the number of grid points. Angles of attack according to Table 5: a) total drag, b) drag decomposed into pressure (upper curves) and friction parts (lower curves).

the DPW-2 conditions, the ANSYS grids have present an opposite tendency to the DLR grids in the prediction of integrated forces with grid refinement. For both configurations and groups of grid, the convergence is monotonic when approaching an infinite resolution. With the DLR grids, the total drag values, as well as its two components, converge asymptotically with second-order accuracy indicated by a straight line for each configuration. This is true also for the WB-FX2B configuration with the ANSYS grids. The WB configuration, however, does not converge with the same accuracy using the ANSYS grid. This is most obvious when considering the two drag components for which the slope is altered. The total drag converges in opposite directions, increasing with the DLR grid refinement and decreasing with the ANSYS grid refinement. Moreover, the difference between the two configurations is larger with the DLR grids than with the ANSYS grids.

To measure the quality of the predictions a measure-of-merit (MOM) was introduced in the summary of the workshop [14]. It is based on Richardson extrapolation of the drag components to a continuum from the fine to the medium grids and from the medium to the coarse grid,

$$y_{\mathrm{FM}} = \frac{X_M y_F - X_F y_M}{X_M - X_F}, \qquad y_{\mathrm{MC}} = \frac{X_C y_M - X_M y_C}{X_C - X_M} \tag{1}$$
$$D(y) = |y_{\mathrm{FM}} - y_{\mathrm{MC}}|$$

where y_{FM} and y_{MC} represent the continuum estimates using the fine-medium and medium-coarse data, respectively, and where $X = N^{-2/3}$ represents a characteristic length in the grid with N being the number of grid points. The measure-of-merit is defined as the sum of the continuum estimates of the two drag components

$$\mathrm{MOM} = D(C_{D\ \mathrm{pressure}}) + D(C_{D\ \mathrm{friction}})$$
$$\mathrm{AvgMOM} = \frac{1}{2}(\mathrm{MOM}_{\mathrm{WB}} + \mathrm{MOM}_{\mathrm{WB-FX2B}}) \tag{2}$$

where AvgMOM is the average measure of the two configurations. With such a definition, grid convergence along a straight line returns a zero value of MOM with second-order accuracy, provided that a uniform mesh refinement is used. Hence, a higher MOM value indicates a degraded grid convergence.

Table 5 contains the continuum values of the drag and its components based on Richardson extrapolation from the fine-medium grids together with the measures-of-merit, MOM and AvgMOM. An exceptionally low MOM value is obtained for the WB-FX2B configuration with the ANSYS grids. The WB configuration, on the other hand, gives a relatively high MOM value and consequently a larger AvgMOM. This is due to the shift in the slope of the grid convergence curves in Fig. 8. The situation is completely different with the DLR grids. Relatively low and very similar values are obtained for both configurations. This gives, accordingly, a rather low AvgMOM with the DLR grid, namely, AvgMOM = 0.00037. Although not included in the DPW-3 summary, this value enables the results with the DLR grids to enter into the top group of the quality ranking.

The continuum drag values show that there is only about one drag count difference obtained with the ANSYS grid between the two configurations. With the DLR grid, however, there is a difference of 11 drag counts. The drag for the WB configuration is higher with the DLR grid, about 18 drag counts. For the WB-FX2B configuration, however, the difference is only about five counts. The different behavior of the grid convergence and the continuum drag values suggests that the solution is very sensitive to the grid used.

Figure 9 presents the integrated forces obtained with the medium grids on both configurations. The difference is observable in the predictions for different configurations and grids. With the WB configuration, the ANSYS grids produce larger lift for all angles of attack computed, which is similar to the computation at $Re = 3 \times 10^6$, as shown in Fig. 5. With the WB-FX2B configuration, both sets of grids have given very similar predictions for the lift. As will be shown next, it is confirmed, with both the ANSYS and DLR grids, that the addition of the fairing in the WB-FX2B configuration is able to remove the separation bubble in the wing–body junction. The reduced difference (from the WB configuration to the WB-FX2B configuration) in the lift predictions may imply that the prediction of the integrated forces may to a large extent be justified by

Table 5 Continuum drag estimates at $C_L = 0.5$ and measure-of-merits

Grid	Configuration	C_D	$C_{D\ \mathrm{pressure}}$	$C_{D\ \mathrm{friction}}$	MOM	AvgMOM
ANSYS	WB	0.02711	0.01375	0.01334	0.00178	0.00094
	WB-FX2B	0.02726	0.01469	0.01256	0.00009	
DLR	WB	0.02894	0.01599	0.01338	0.00038	0.00037
	WB-FX2B	0.02782	0.01441	0.01340	0.00036	

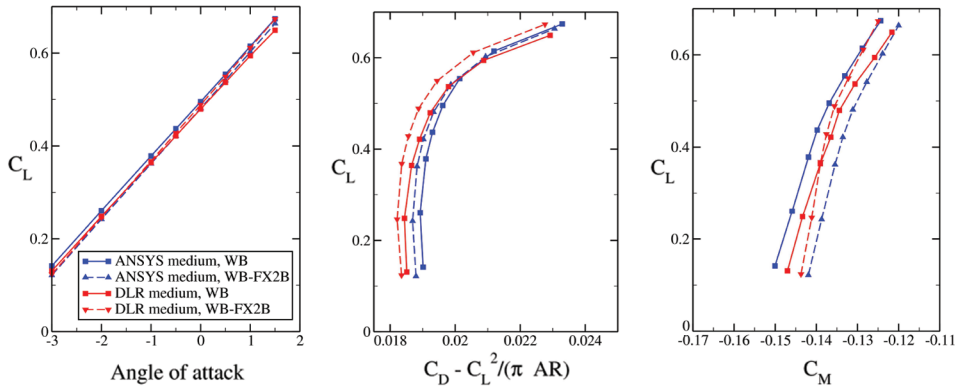

Fig. 9 Integrated forces and moments for the WB, WB-FX2B, with ANSYS and DLR grids, $Re = 5 \times 10^6$: a) C_L vs α, b) lift-drag polar with induced drag subtracted, c) C_L vs C_M.

the prediction of the flow separation in the wing–body junction. The drag prediction is, however, much more sensitive to the two sets of grids and to the two different configurations. With both the ANSYS and DLR grids, the drag is reduced with the fairing due to the elimination of the separation region, as compared with the no-fairing WB configuration. This is particularly the case with the DLR grids, and holds true at small angles with the ANSYS grids. With the same configuration, the ANSYS grids have produced generally larger drag than the DLR grids, but not for the WB configurations at large angles of attack (where the DLR grid yields, instead, slightly larger drag values than the ANSYS grid).

The pitching moment shows similar behavior for the WB configuration as for the DPW-2 conditions, as illustrated in Fig. 5, but the gap between the two curves has slightly increased. With the WB-FX2B configuration, the moment shifts to negatively smaller values with the ANSYS grids. With the DLR grids, such a shift happens only at small angles and the pitching moment becomes larger (with a negative sign) at large angles when the fairing is added. The difference in the predictions of drag and pitching moment for the WB-FX2B configuration indicates the importance of the grid resolution even for attached flows.

The effect of Reynolds number is illustrated in Fig. 10 by plotting the lift and the drag as a function of α. The integrated forces are plotted for both Reynolds numbers computed, respectively, with the ANSYS and DLR grids for the WB configuration. At $Re = 3 \times 10^6$, the experimental data have also been plotted as a reference. It is shown that changing the Reynolds number from $Re = 3 \times 10^6$ to $Re = 5 \times 10^6$ has increased the lift but reduced the drag. Both the ANSYS and DLR grids have shown a similar tendency on the effect of Reynolds number, although the predicted lift and drag are different at the same Reynolds number due to the different sets of grids. The lift obtained with the DLR grid at $Re = 5 \times 10^6$ is collapsed to the prediction obtained with the ANSYS grid at $Re = 3 \times 10^6$.

The pressure distributions at $\alpha = 1$ deg is presented in Fig. 11 at four spanwise wing sections. Four sets of solutions have been compared in the illustrations. These are computed, respectively, with the ANSYS and DLR medium grids for both WB and WB-FX2B configurations. The major differences are again observed at the most inboard station at 15% span. The solutions for the WB configuration on the two grids give quite different pressure distributions, similar to what has been found at $Re = 3 \times 10^6$ in Fig. 6. This is due to the flow separation region in the wing–body junction, which has been predicted differently with the two grids. Again, the DLR grid has pronounced a more extended separation bubble than the ANSYS grid. For the WB-FX2B configuration, the two grids give almost identical pressure distribution at this section, because both grids have disclosed the absence of the separation bubble due to the addition of the fairing. At outboard stations, the differences between the solutions are marginal for both configurations on the two grids. This indicates that the fairing added in the wing–body junction has little effect on the flow properties over the outboard wing surface, and that the two grids have induced similar resolutions on the boundary layer attached on the wing surface. Nevertheless, some visible differences can be observed at and near the location of the shock, due to the difference in the grids and in the configuration. At 24% span for the WB configuration, the DLR grid has produced a slightly earlier shock location and a larger pressure on the suction side after the shock than the ANSYS grid. The prediction of an early shock

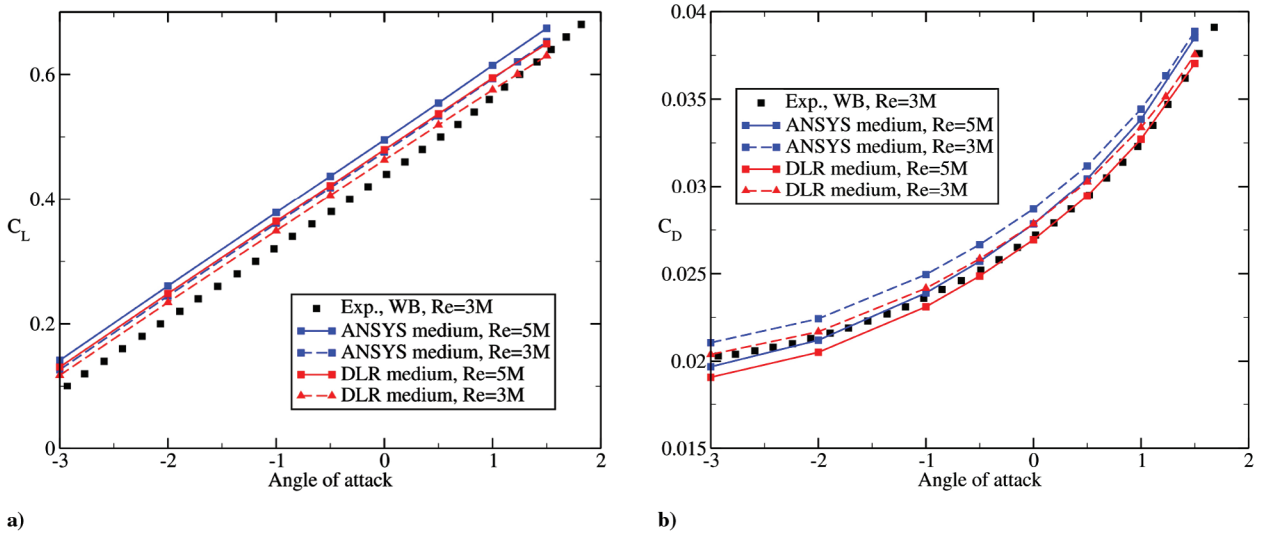

Fig. 10 Total lift and drag for the WB configuration at $Re = 5 \times 10^6$ and $Re = 3 \times 10^6$: a) C_L vs α, b) C_D vs α.

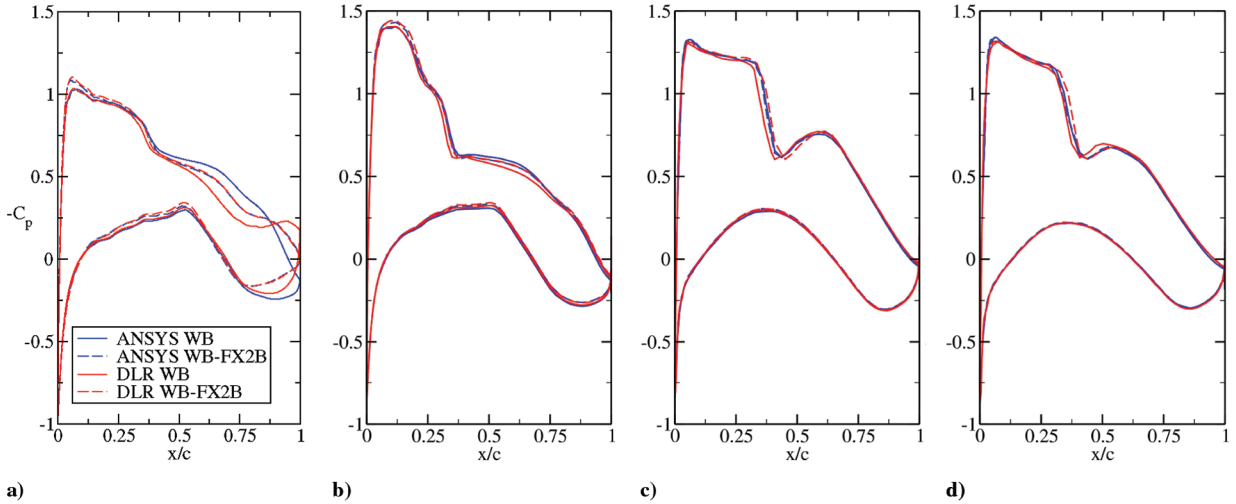

Fig. 11 Pressure distributions for the WB and WB-FX2B configurations on the ANSYS and DLR medium grids for $\alpha = 1$ deg and $Re = 5 \times 10^6$: a) 15% span, b) 24% span, c) 41% span, d) 64% span.

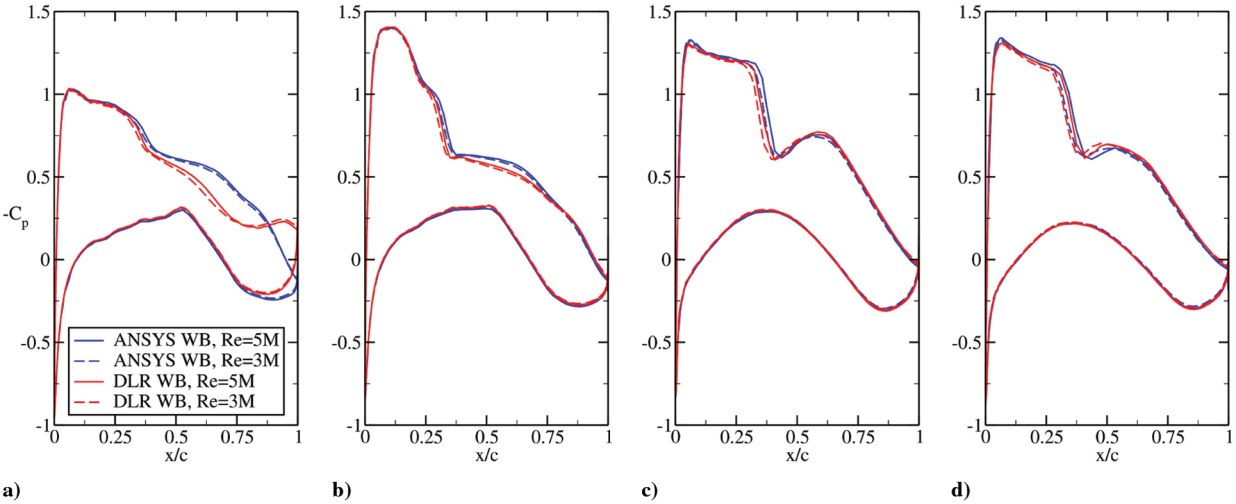

Fig. 12 Pressure distributions for the WB configuration on the ANSYS and DLR medium grids at $Re = 5 \times 10^6$ and $Re = 3 \times 10^6$ for $\alpha = 1$ deg: a) 15% span, b) 24% span, c) 41% span, d) 64% span.

location is present also at 41% span for the WB configuration on the DLR grid. At the 64% span section, on the other hand, the DLR grid has yielded a slightly delayed shock for the WB-FX2B. Apart from the aforementioned difference, in general, all the solutions have claimed similar shock location for both the WB and WB-FX2B configurations. As mentioned, along with the grid resolution, the somewhat early triggered shock at the most inboard section (15% span) for the WB configuration on the DLR grid may be associated to the prediction of downstream flow separation in the wing–body junction. Such an early (slightly though) shock location remains in the predictions at 24 and 41% span sections. This may imply that the separation in the downstream junction has imposed some effects on the flow at these outboard stations.

To observe the effect of Reynolds number, Fig. 12 presents the pressure distributions for the WB configuration computed using both the DLR and ANSYS grids for $Re = 3 \times 10^6$ and $Re = 5 \times 10^6$, respectively. Again, the main difference has been caused by the grids at the same Reynolds number. At different Reynolds numbers with the same grid, however, the pressure distributions are very similar, though a slight difference is visible. As observed repeatedly in the preceding presentation, the difference in the prediction of the downstream junction flow separation has been preserved, respectively, for the ANSYS and DLR grids. The same holds also for the prediction of the shock, for which the DLR grid predicts an earlier shock than the ANSYS grid at the same Reynolds number. Nevertheless, with the same set of grid (DLR or ANSYS), the change of Reynolds number has altered the predicted shock location, which is shifted downstream as the Reynolds number increases.

To shed a light on the difference in the pressure distribution at the most inboard section (15% span), Fig. 13 illustrates the surface friction pattern in the downstream wing–body junction based on four numerical solutions at $\alpha = 0$ deg. The flow patterns for the WB configuration are obtained with the DLR medium grid at $Re = 3 \times 10^6$ and $Re = 5 \times 10^6$, respectively, and at $Re = 3 \times 10^6$ with the ANSYS medium grid. The flow pattern is presented for the WB-FX2B configuration at $Re = 5 \times 10^6$ with only the DLR medium grid (the ANSYS grid gives very similar surface friction pattern). The simulated patterns are compared with the oil pattern visualized experimentally by ONERA for DPW-2 (at $Re = 3 \times 10^6$). The angle of attack of $\alpha = 0$ deg has been chosen at which $C_L \approx 0.5$ is predicted. It should be noted that the experimental pattern was visualized for the WB configuration including a pylon and a nacelle at an angle of attack with $C_L \approx 0.5$, which occurs at $\alpha = 0$ deg.

As shown in Figs. 13b and 13d, the DLR grid has resolved the flow separation bubble at both Reynolds numbers considered. The separation starts at about 70% of the local chord and is more extended than the separation visualized by the experiment. The predicted separation moves slightly downstream at $Re = 5 \times 10^6$. With the ANSYS grid, however, the separation bubble is hardly visible in Fig. 13c, which is indeed very small and weak, as already illustrated

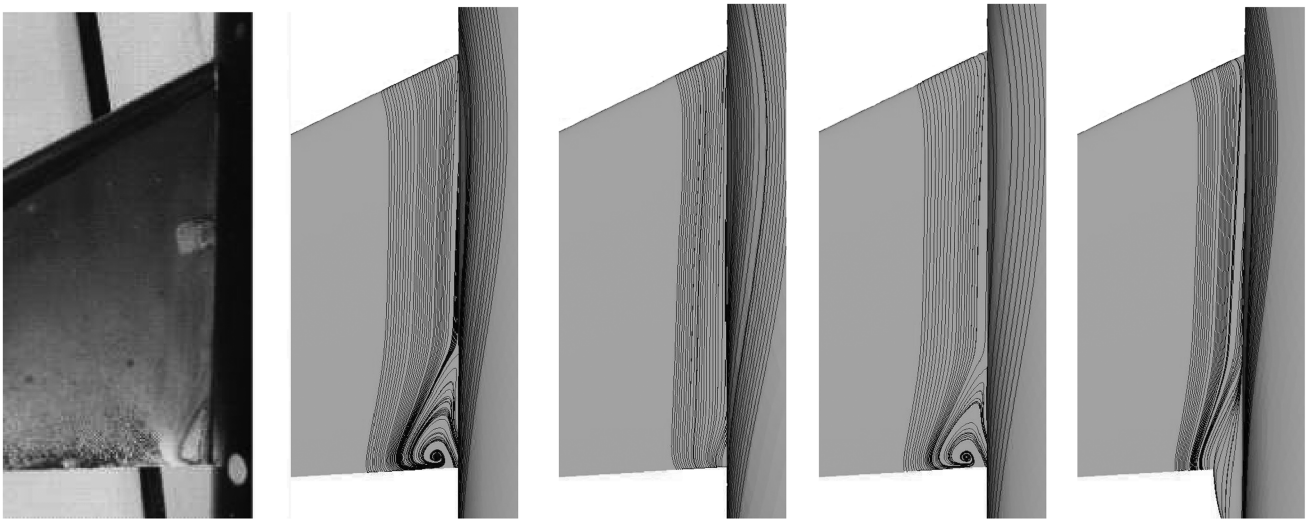

a) b) c) d) e)

Fig. 13 Surface friction pattern at angle of attack $\alpha = 0$ deg: a) experimental oil flow visualization, WB, $Re = 3 \times 10^6$; b) DLR medium grid, WB, $Re = 3 \times 10^6$; c) ANSYS medium grid, WB, $Re = 3 \times 10^6$; d) DLR medium grid, WB, $Re = 5 \times 10^6$; e) DLR medium grid, WB-FX2B, $Re = 5 \times 10^6$.

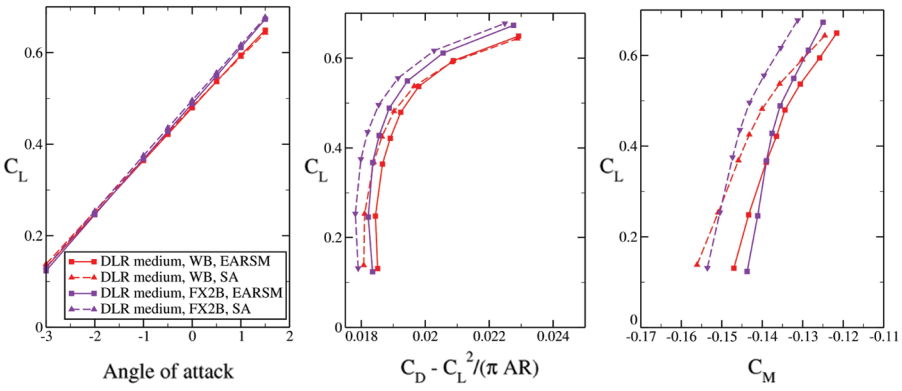

a) b) c)

Fig. 14 Integrated forces and moments for the WB and WB-FX2B configurations. DLR medium grid is used with two turbulence models at $Re = 5 \times 10^6$: a) C_L vs α, b) lift-drag polar with induced drag subtracted, c) C_L vs C_M.

in Fig. 7. For the WB-FX2B configuration, all the grids have claimed in the predictions that this separation bubble is removed due to the addition of the fairing, as shown in Fig. 13e as an example with the DLR medium grid at $Re = 5 \times 10^6$. The difference in the predicted separation has been reflected consistently in the pressure distributions at 15% span section in Figs. 6, 11, and 12. The separation predicted by the DLR grid is too much extended in the spanwise direction for the WB configuration, which has caused the discrepancy from the experimental data for the pressure distribution at 15% span, as shown in these figures.

The Spalart–Allmaras turbulence model has been one of the commonly used modeling approaches in aeronautic applications, and has been used by many DPW-3 participants. For comparison, the SA model has also been adopted in the present work. In this case, the DLR medium grid has been employed for both configurations at $Re = 5 \times 10^6$.

Figure 14 presents the integrated forces and moments computed by the SA model in comparison with the results obtained with the EARSM. The predicted lift is very similar for the same configuration with different models. The predicted drag is, however, sensibly different. For the WB-FX2B configuration, the EARSM produces larger drag than the SA model for all the angles considered, whereas the difference between the drag predictions with the two models has been diminished for the WB configuration with increasing angle of attack. Significant influence is observed in the pitching moment, for which the EARSM gives generally smaller (with a negative sign) predictions than the SA model for both configurations. The solution with the SA model is further analyzed next in comparison with the EARSM.

In Fig. 15, the pressure distributions at $\alpha = 0$ deg are compared for the two turbulence models and configurations. For the WB-FX2B configuration, where the boundary layer is attached over the wing surface, the two models have produced nearly identical results. This suggests that the SA model and the EARSM possess a very similar behavior in predictions of attached turbulent boundary-layer flows. Visible difference arises, however, for the WB configuration in modeling the flow separation in the wing–body junction, as illustrated at the inboard station at 15% wing span. The surface pressure predicted by the SA model is somewhat larger than the EARSM after the shock location, and is smaller in the separation region near the wing trailing edge. The shock positions are very similar, being pronounced by both models for the same configuration. The most obvious difference in the pressure distributions has been induced due to different configurations. The attached flow in the WB-FX2B configuration has moved the shock position slightly further downstream, as compared with the shock location predicted for the WB configuration.

Figure 16 displays further the surface friction pattern in the wing–body junction. As seen, both models have captured the separation bubble with a similar extension in the streamwise direction. The location of the recirculation *eye* on the wing surface is, however, somewhat different, which is slightly moved upstream in the

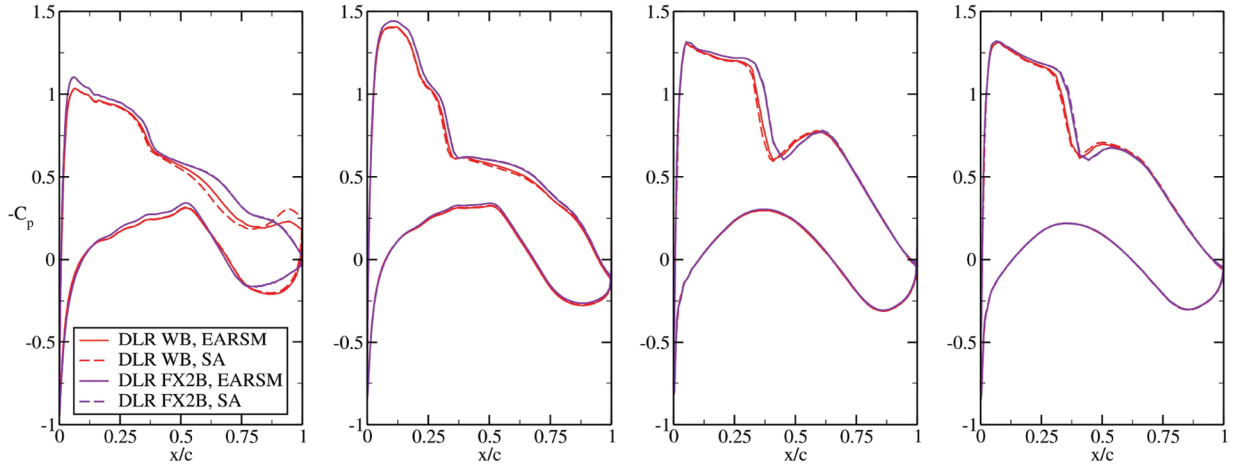

Fig. 15 Pressure distributions with EARSM and SA model for the WB and WB-FX2B configurations with DLR medium grid for $\alpha = 1$ deg and $Re = 5 \times 10^6$: a) 15% span, b) 24% span, c) 41% span, d) 64% span.

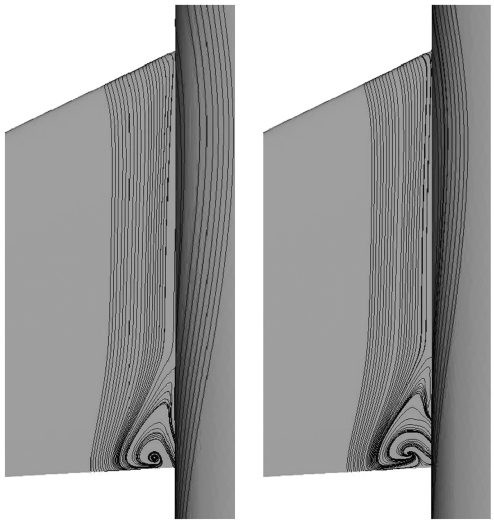

Fig. 16 Surface friction pattern at angle of attack $\alpha = 0$ deg, $Re = 5 \times 10^6$ DLR medium WB grid: a) EARSM, b) SA model.

prediction by the SA model. This implies that the SA model has yielded a relatively extensive flow separation with a strong backflow near the wing surface. This corresponds to the pressure distributions presented in Fig. 15 at the 15% wing span, which indicates that the SA model has produced a slightly larger adverse pressure gradient near the wing trailing edge. Obviously, the two models have their major difference incurred in modeling flow separation for the case considered. When the effect of flow separation is insignificant on the overall flow properties, the two models give similar predictions for the integrated forces and pressure distributions. In view of the computed results in the present work, it is noted that the major difference between the solutions is rooted in the grids used. The influence due to the turbulence model is relatively smaller than the influence from the selected grid type.

The question is, then, why the two groups of grids provide rather different flow solutions (for the WB configuration), particularly in resolving the wing–body junction flow separation. The answer to this is not very clear. In an early work for DPW-2 with the WB configuration by Mavriplis [12], for example, a similar situation has been observed. With two different groups of grids, both are well converged and refined (up to 72 million nodes), Mavriplis showed that one grid (with 65 million nodes) gives lower lift than the other group of grids, and that the prediction coincides with the experimental values at larger angles of attack. This is similar to the results obtained in the present work with the DLR grid (on top of the experimental lift values at large angles) and the ANSYS grid (overprediction of the lift for all angles).

One plausible explanation for the difference between the solutions may be traced to the meshing over the near-wall prismatic layer. An interesting observation is that the DLR WB grids, which produce relatively extensive flow separation in the wing–body junction and give predictions in improved agreement with measured forces and moments, contain a constant number of near-wall prismatic layers with no pyramid elements for the transition to off-wall tetrahedral elements. The ANSYS grids, on the other hand, have a varying number of prismatic elements, as shown in Fig. 3 and in Tables 1 and 2. This is similar to the grids used by Mavriplis [12], where the grid with 65 million nodes has a constant number of prismatic layers with no pyramids and, similarly, also gives improved predictions for the integrated forces and moments, in contrast to the results given by the other group of grids (with 72 million nodes) with a varying number of near-wall prismatic cells. If such an observation is justifiable, this is most likely a numerical issue related to the spatial discretization technique on the median dual grids.

IV. Conclusions

Numerical calculations have been performed and summarized for the Third AIAA Drag Prediction Workshop (DPW-3). Two configurations have been investigated, a clean wing–body configuration (WB) being the same as in DPW-2 and the same configuration with a fairing (WB-FX2B) added in the wing–body junction near the wing trailing edge. The WB-FX2B configuration is designed to remove the flow separation in this area. The computations have been conducted for a sweep of angles of attack. A grid refinement study has also been performed. The calculations are carried out for fully developed turbulent flow at a freestream Mach number of $M_\infty = 0.75$ and a Reynolds number of $Re = 5 \times 10^6$. Two groups of hybrid unstructured grids, generated by ANSYS and DLR, have been used, involving 12 grids in the analysis, that is, three grids (with different sizes) for each configuration due to the two different grid groups. The CFD-solver Edge has been employed for the investigation.

There is no experimental data available for the DPW-3 flow conditions. To validate the numerical and physical settings implemented in the solver, a number of computations have been undertaken for the WB configuration based on the DPW-2 flow conditions in comparison with existing experimental data measured at $Re = 3 \times 10^6$ and $M_\infty = 0.75$. The calculations on both groups of grids converge well to steady solutions, which have shown generally reasonable agreement with the experimental data. Similar to many

DPW-2 contributions by other participants, the lift is slightly overpredicted. The ANSYS group of grids gives somewhat more deviated predictions from the measured data, as compared with the results obtained with the DLR group of grids which has produced lift predictions in line with the experimental measurements at large angles. For the drag and pitching moment, the DLR grids also give better predictions than the ANSYS grid. Moreover, the two groups of grids have induced very different resolution on the flow separation arising in the wing–body junction near the trailing edge. The ANSYS grids have produced a very small and weak separation bubble, whereas the flow separation has been disclosed much more extensively by the DLR grids.

With the DPW-3 flow conditions, generally reasonable predictions have been achieved for both configurations on the two groups of grids. Nevertheless, similar differences remain for the WB configuration between the two groups of grids, being observed in the predictions of integrated forces and pitching moment, the pressure distributions, as well as the flow separation. In the analysis of grid sensitivity, the two groups of grids show asymptotic convergence but with an opposite tendency. With grid refinement, the ANSYS grids produce reduced drag, whereas the drag is increased with the DLR grids. The major difference in the predictions is due to the different groups of grids. For the same configuration (WB or WB-FX2B), the ANSYS grids give larger drag and pitching moment (negatively) than the DLR grids, though the difference in lift predictions is marginal. The addition of the fairing in the WB-FX2B configuration has eliminated the separation bubble in the wing–body junction. With both the DLR and ANSYS grids, attached flow is reproduced over the wing surface. The pressure distributions at different wing sections are thus very similar for this configuration due to the two groups of grids, whereas for the WB configuration, the prediction for the wing–body junction flow separation has induced different pressure distributions with different grids. In addition, the addition of the fairing gives little effect on the lift prediction, but at large α, marginally larger lift is predicted than for the WB configuration. Furthermore, the fairing has reduced the drag and, at large α, has increased the pitching moment (with negative value), although being reduced at small α.

The result obtained with the DLR grids is better than with the ANSYS grids. This is in line with the monotonic and second-order asymptotic grid convergence obtained for both configurations with the DLR grids. The grid convergence is satisfactory also for the ANSYS grids on the WB-FX2B configuration. For the WB configuration, however, the accuracy of the ANSYS grid convergence is degraded. The measure-of-merit (MOM), introduced in the DPW-3 summary to measure the linearity of the grid convergence, underlines this observation.

In the analysis on the effect of Reynolds number, it is found that the lift is increased and the drag is reduced when the Reynolds number is increased from $Re = 3 \times 10^6$ to $Re = 5 \times 10^6$ for both configurations. With the same configuration, on the other hand, only a small variation has been observed for the wing pressure distribution, most visibly for the predicted shock position. The low Reynolds number has brought the shock slightly further upstream than at the high Reynolds number. The flow separation in the wing–body junction with the WB configuration is hardly affected by the Reynolds number when the same group of grids is used.

The effect of turbulence modeling arises in the prediction of flow separation. In regions on the wing surface where the flow is attached, the SA model gives pressure distributions very similar to those given by the EARSM. Nevertheless, visible variation has been detected in the predictions for the drag and pitching moment for both configurations. In general, the SA model produces larger drag and smaller pitching moment than the EARSM. Furthermore, the SA model has predicted a relatively extensive separation in the wing–body junction. In the present work, it is found that the effect of the turbulence model is small, relative to the influence of the different groups of grids.

In general, high-quality predictions have been attained in the present computations for both configurations. Nonetheless, variation in the predictions due to two different groups of grids needs to be further scrutinized. This has been plausibly attributed to the varying numbers of near-wall prismatic layers nestled in the ANSYS grid. It may in turn be related to the numerical discretization on the dual grids for different types of element in the boundary layer. Examination on this numerical issue will be performed further in the future.

Acknowledgments

The authors are grateful to ANSYS and DLR for providing the unstructured grids used for the investigation in this paper.

References

[1] Peng, S.-H., and Eliasson, P., "Comparison of Turbulence Models in Prediction of Flow Around the DLR F6 Aircraft Configuration," AIAA Paper 2004-4718, 2004.

[2] Peng, S.-H., "Numerical Computations on the DLR-F6 Aircraft Configuration Using Different Turbulence Models," FOI Scientific Rept. FOI-R-1154-SE, 2004.

[3] Laflin, K. R., Vassberg, J. C., Wahls, R. A., and Morrison, J. H., "Summary of Data from the Second AIAA CFD Drag Prediction Workshop (Invited)," AIAA Paper 2004-555, 2004.

[4] Hemsch, M. J. A., and Morrison, J. H., "Statistical Analysis of CFD Solutions from 2nd Drag Prediction Workshop (Invited)," AIAA Paper 2004-556, 2004.

[5] Yamamoto, K., Ochi, A., Shima, E., and Takaki, R., "CFD Sensitivity of Drag Prediction on DLR-F6 Configuration by Structured Method and Unstructured Method," AIAA Paper 2004-398, 2004.

[6] Klausmeyer, S., "Drag, Lift and Moment Estimates of Transonic Aircraft Using the Navier–Stokes Equations," AIAA Paper 2004-553, 2004.

[7] Brodersen, O., Rakowitz, M., Amant, S., Larrieu, P., and Sutcliffe, M., "Airbus, ONERA and DLR Results from the 2nd AIAA Drag Prediction Workshop," AIAA Paper 2004-391, 2004.

[8] Tinoco, E., and Su, T., "Drag Prediction with the Zeus/CLF3D System," AIAA Paper 2004-552, 2004.

[9] Langtry, R., Kuntz, M., and Menter, F., "Drag Prediction of Engine-Airframe Interference Effects with CFX 5," AIAA Paper 2004-392, 2004.

[10] Rumsey, C. L., Rivers, S. M., and Morrison, J. H., "Study of CFD Variation on Transport Configurations from the Second Drag-Prediction Workshop," *Computers and Fluids*, Vol. 34, No. 7, 2005, pp. 785–816.
doi:10.1016/j.compfluid.2004.07.003

[11] Baker, T. J., "Parsing the Results of the Second Drag Prediction," AIAA Paper 2005-4731, 2005.

[12] Mavriplis, D. J., "Grid Resolution Study of a Drag Prediction Workshop Configuration Using the NSU3D Unstructured Mesh Solver," AIAA Paper 2005-4729, 2005.

[13] Vassberg, J. C., Sclafani, A. J., and DeHaan, M. A., "Wing-Body Fairing Design for the DLR-F6 Model: A DPW-3 Case Study," AIAA Paper 2005-4730, 2005.

[14] Vassberg, J. C., Tinoco, E. N., Mani, M., Brodersen, O. P., Eisfeld, B., Wahls, R. A., Morrison, J. H., Zickuhr, T., Laflin, K. R., and Mavriplis, D. J., "Summary of the Third AIAA Drag Prediction Workshop," AIAA Paper 2007-0260, 2007.

[15] Eliasson, P., "EDGE, a Navier–Stokes Solver for Unstructured Grids," FOI Rept. FOI-R-0298-SE, 2005.

[16] Eliasson, P., "EDGE, a Navier–Stokes Solver for Unstructured Grids," *Finite Volumes for Complex Applications 3: Problems and Perspectives*, Hermes Penton Science, London, 2002, pp. 527–534.

[17] Berglind, T., "Agglomeration Algorithm for Navier–Stokes Grids," AIAA Paper 2000-2254, 2000.

[18] Haselbacher, A., McGuirck, J. J., and Page, G. J., "Finite Volume Discretization Aspects for Viscous Flows on Mixed Unstructured Grids," *AIAA Journal*, Vol. 37, No. 2, Feb. 1999, pp. 177–184.

[19] Hellsten, A., "New Advanced k-ω Turbulence Model for High Lift Aerodynamics," *AIAA Journal*, Vol. 43, No. 9, 2005, pp. 1857–1869.

[20] Spalart, P. R., and Allmaras, S. R., "One-Equation Turbulence Model for Aerodynamic Flows," AIAA Paper 92-0439, 1992.